

Light Water Reactor Sustainability Program

A Demonstration of Concrete Structural Health Monitoring Framework for Degradation due to Alkali-Silica Reaction



April 2016

U.S. Department of Energy

Office of Nuclear Energy

DISCLAIMER

This information was prepared as an account of work sponsored by an agency of the U.S. Government. Neither the U.S. Government nor any agency thereof, nor any of their employees, makes any warranty, expressed or implied, or assumes any legal liability or responsibility for the accuracy, completeness, or usefulness, of any information, apparatus, product, or process disclosed, or represents that its use would not infringe privately owned rights. References herein to any specific commercial product, process, or service by trade name, trade mark, manufacturer, or otherwise, does not necessarily constitute or imply its endorsement, recommendation, or favoring by the U.S. Government or any agency thereof. The views and opinions of authors expressed herein do not necessarily state or reflect those of the U.S. Government or any agency thereof.

Light Water Reactor Sustainability Program

Sankaran Mahadevan
Vivek Agarwal
Kyle Neal
Paromita Nath
Yanqing Bao
Guowei Cai
Peter Orme
Douglas Adams
David Kosson

April 2016

Vanderbilt University
Nashville, Tennessee 37235

Idaho National Laboratory
Idaho Falls, Idaho 83415

Prepared for the
U.S. Department of Energy
Office of Nuclear Energy
Under DOE Idaho Operations Office
Contract DE-AC07-05ID14517

ABSTRACT

Assessment and management of aging concrete structures in nuclear power plants require a more systematic approach than simple reliance on existing code margins of safety. Structural health monitoring of concrete structures aims to understand the current health condition of a structure based on heterogeneous measurements to produce high-confidence actionable information regarding structural integrity that supports operational and maintenance decisions.

This ongoing research project is seeking to develop a probabilistic framework for a health diagnosis and prognosis of aging concrete structures in a nuclear power plant that is subjected to physical, chemical, environmental, and mechanical degradation. The proposed framework consists of four elements: monitoring, data analytics, uncertainty quantification, and prognosis. This report focuses on degradation caused by alkali-silica reaction (ASR). Controlled specimens were prepared to develop accelerated ASR degradation. Different monitoring techniques (i.e., thermography, digital image correlation, mechanical deformation measurements, nonlinear impact resonance acoustic spectroscopy, and vibro-acoustic modulation) were used to detect the damage caused by ASR. Heterogeneous data from multiple techniques were used for damage diagnosis and prognosis and quantification of the associated uncertainty using a Bayesian network approach. Additionally, the MapReduce technique has been demonstrated with synthetic data. This technique can be used in the future to handle large amounts of observation data obtained from online monitoring of realistic structures.

EXECUTIVE SUMMARY

One challenge for the current fleet of light water reactors in the United States is age-related degradation of their passive assets that include concrete, cables, piping, and the reactor pressure vessel. As the current fleet of nuclear power plants (NPPs) continues to operate up to 60 years or beyond, it is important to understand the current and the future health condition of passive assets under different operating conditions that would support operational and maintenance decisions. To ensure long-term safe and reliable operation of the current fleet, the U.S. Department of Energy's Office of Nuclear Energy funds the Light Water Reactor Sustainability Program to develop the scientific basis for extending operation of commercial light water reactors beyond the current license extension period.

Among the different passive assets of interest in NPPs, concrete structures are investigated in this research project. Reinforced concrete structures found in NPPs can be grouped into four categories: (1) primary containment, (2) containment internal structures, (3) secondary containments/reactor buildings, and (4) spent fuel pool and cooling towers. These concrete structures are affected by a variety of degradation mechanisms that are related to chemical, physical, and mechanical causes and to irradiation. Age-related degradation of concrete results in gradual microstructural changes (e.g., slow hydration, crystallization of amorphous constituents, and reactions between cement paste and aggregates). Changes over long periods of time must be measured, monitored, and analyzed to best support long-term operation and maintenance decisions.

Structural health monitoring of concrete structures aims to understand the current health condition of a structure based on the heterogeneous measurements for producing high-confidence actionable information regarding structural integrity and reliability. To achieve this research objective, Vanderbilt University, in collaboration with Idaho National Laboratory and Oak Ridge National Laboratory, is developing a probabilistic framework for the health monitoring of NPP concrete structures subject to physical, chemical, and mechanical degradation. A systematic approach that is proposed to assess and manage aging concrete structures requires an integrated framework, including four elements: (1) monitoring, (2) data analytics, (3) uncertainty quantification, and (4) prognosis.

A proof-of-concept example of this framework was reported in March 2015, using a small concrete slab and aggressive freeze-thaw cycling. Effective combinations of full-field monitoring techniques and related data analytics and diagnosis/prognosis techniques need to be identified for different types of concrete structures under different loading and operating conditions. This report focuses on degradation caused in concrete by alkali-silica reaction (ASR). Specimens with ASR degradation are prepared to demonstrate the framework using several monitoring techniques at Vanderbilt University's Laboratory for Systems Integrity and Reliability. The measured data are linked to a probabilistic framework; the monitoring data are input to a Bayesian network for information fusion, uncertainty quantification of a diagnosis result, and prognosis. Additionally, the MapReduce technique is implemented to handle large amounts of observation data in order to facilitate implementation of continuous online monitoring of realistic NPP structures.

Some of the outcomes of this proof of concept demonstration are as follows:

1. Small ($9 \times 5 \times 2$ -in.) and medium ($24 \times 24 \times 6$ -in.)-sized controlled specimens were prepared and cured to produce accelerated ASR degradation.
2. The specimens were investigated using various monitoring techniques: thermography, digital image correlation, mechanical deformation measurements, nonlinear impact resonance acoustic spectroscopy, and vibro-acoustic modulation.
3. Data analytics results from multiple monitoring techniques were used as inputs to a Bayesian network for information fusion and uncertainty quantification of the diagnosis result.
4. A coupled thermos-hydro-mechanical-chemical model implemented in Abaqus in the form of a user-developed subroutine (UMAT) was used for prognosis.
5. The MapReduce technique was implemented and demonstrated to parallelize the Markov chain Monte Carlo used for Bayesian updating for uncertainty quantification in order to facilitate handling of big data resulting from continuous online monitoring of realistic structures.

The methodologies described in this milestone report are focused on concrete structural health monitoring measurements, data analytics, and uncertainty quantified diagnosis, and prognosis. This will support continuous assessment of concrete performance. The proof-of-concept demonstration presented in this report highlights the significance of each element of the framework and its integration.

During the next phase of research, monitoring techniques will be refined for detection and localization of ASR in a reinforced concrete specimen. The uncertainty quantification approaches and integration framework will be advanced further to handle large amounts of observation data. The resulting comprehensive approach will facilitate development of a quantitative, risk-informed framework that would be generalizable for a variety of concrete structures.

ACKNOWLEDGMENTS

This report was made possible through funding by the U.S. Department of Energy's Light Water Reactor Sustainability Program. We are grateful to Richard Reister of the U.S. Department of Energy and Bruce Hallbert and Kathryn McCarthy at Idaho National Laboratory for championing this effort. We also thank Jodi Vollmer at Idaho National Laboratory for technical editing and formatting of the report.

CONTENTS

ABSTRACT.....	v
EXECUTIVE SUMMARY	vii
ACKNOWLEDGMENTS	ix
ACRONYMS.....	xv
1. INTRODUCTION	1
1.1 Background	1
1.1.1 Monitoring	2
1.1.2 Data Analytics	2
1.1.3 Uncertainty Quantification	2
1.1.4 Prognosis.....	3
1.2 Report Layout.....	3
2. EXPERIMENTAL STUDY	3
2.1 Sample Preparation and Curing	3
2.1.1 Cement Bricks	3
2.1.2 Cement Slab.....	6
2.2 Non-Destructive Examination Techniques	9
2.2.1 Infrared Thermography.....	9
2.2.2 Digital Image Correlation.....	9
2.2.3 Mechanical Deformation Measurement.....	10
2.2.4 Non-Linear Impact Resonance Acoustic Spectroscopy.....	10
2.2.5 Vibro-Acoustic Modulation.....	10
2.3 Non-Destructive Examination Experimental Setup	11
2.3.1 Infrared Thermography Experimental Setup	11
2.3.2 Digital Image Correlation Setup.....	13
2.3.3 Mechanical Deformation Measurements	14
2.3.4 Set Up of Non-Linear Impact Resonance Acoustic Spectroscopy	15
2.3.5 Vibro-Acoustic Modulation Setup.....	16
3. DATA ANALYTICS	16
3.1 Alkali-Silica Reaction Detection in Brick Samples Using Infrared Thermography	16
3.2 Detection Using Nonlinear Impact Resonance Acoustic Spectroscopy.....	17
3.3 Vibro-Acoustic Modulation	19
4. DIAGNOSIS.....	20
4.1 Diagnosis.....	20
4.1.1 Data Fusion.....	20
4.1.2 Results.....	21
4.2 Big Data Analytics	23
4.2.1 MapReduce	23
4.2.2 Parallelization of Markov Chain Monte Carlo.....	24
4.2.3 Results.....	24

5. PROGNOSIS	25
5.1 Alkali-Silica Reaction Finite Element Model	25
5.1.1 Implementation of Saouma and Perotti's Model	25
6. SUMMARY AND FUTURE WORK	30
7. REFERENCES	31

FIGURES

Figure 1. Elements of concrete structural health monitoring.....	2
Figure 2. Sketches of A1/A2 (top), B1/B2 (middle), and C1/C2 (bottom), where the shaded region represents glass slices.	4
Figure 3. Brick B2 showing whitish effluent (ASR gel).....	4
Figure 4. Aggregate type and location in the second batch of samples.	5
Figure 5. Brick Number 6 during casting of the second batch of samples.	5
Figure 6. Stainless steel pegs being inserted during casting.	6
Figure 7. 2-ft × 2-ft × 6-in. cement slab.....	6
Figure 8. Pockets of aggregate labeled in a cement slab during pouring.....	7
Figure 9. 2-ft × 2-ft × 6-in. mold.	8
Figure 10. Slab sitting on the frame being lowered into the tub.	8
Figure 11. Slab being placed in the oven for accelerated curing.	9
Figure 12. VAM representation of system response to pumping signal.	10
Figure 13. Side bands indicating modulation.....	11
Figure 14. The heating blanket's temperature cycle for the bricks.....	12
Figure 15. Small bricks on the thermal heating blanket.....	12
Figure 16. The heating blanket's temperature cycle for the slab.	13
Figure 17. Brick with speckled pattern.	13
Figure 18. Results from DIC.....	14
Figure 19. Calipers used for mechanical deformation measurements.	14

Figure 20. Measuring the distance between nails on a brick.	14
Figure 21. NIRAS test setup.	15
Figure 22. Raw acceleration data from NIRAS.	15
Figure 23. Slab B2 (left) and Slab C2 (right). ASR is indicated by the red areas.....	16
Figure 24. Results from a concrete brick, showing frequency shift with increasing input force amplitude.	17
Figure 25. Calculation of nonlinearity parameter for the brick specimen.	17
Figure 26. Frequency response of the large slab to impact excitation in four locations.	18
Figure 27. Resonant frequency shift of the large to increasing impact force.....	18
Figure 28. VAM results for three concrete bricks.....	19
Figure 29. Bayesian network for data fusion of IR, NIRAS, and VAM.....	21
Figure 30. Bayesian network being used.	21
Figure 31. Updated damage indicator.	22
Figure 32. Damage area updated by NIRAS, VAM, and IR.....	22
Figure 33. MapReduce execution overview.	23
Figure 34. Accuracy of parallelization.....	24
Figure 35. Efficiency of parallelization.	25
Figure 36. ASR detection in C2 (red: ASR).	26
Figure 37. Finite element mesh of C2 brick.....	27
Figure 38. Model initial condition for prognosis (above: full model view; below: cut view).	28
Figure 39. Future prediction of ASR growth (half model).	29
Figure 40. Time history of ASR extent.....	29

TABLES

Table 1. Comparison of VAM and NIRAS results.	19
Table 2. Observations.	22

Table 3. General parameters of the ASR model.	27
--	----

ACRONYMS

ASR	alkali-silica reaction
DIC	digital image correlation
IR	infrared
MCMC	Markov chain Monte Carlo
NaOH	sodium hydroxide
NIRAS	nonlinear impact resonance acoustic spectroscopy
NPP	nuclear power plant
SHM	structural health monitoring
VAM	vibro-acoustic modulation

A Demonstration of Concrete Structural Health Monitoring Framework for Degradation due to Alkali-Silica Reaction

1. INTRODUCTION

Because many existing nuclear power plants (NPPs) continue to operate beyond their license life, plant structures, systems, and components suffer deterioration that affects their structural integrity and performance. Health monitoring is an essential technology for ensuring the current and future state of a NPP will meet the performance and safety requirements. This project focuses on concrete structures in NPPs. The concrete structures are grouped into the following four categories: (1) primary containment, (2) containment internal structures, (3) secondary containment/reactor buildings, and (4) other structures such as used fuel pools, dry storage casks, and cooling towers. These concrete structures are affected by a variety of chemical, physical, and mechanical degradation mechanisms such as alkali-silica reaction (ASR), chloride penetration, sulfate attack, carbonation, freeze-thaw cycles, shrinkage, and mechanical loading (Naus 2007). The age-related deterioration of concrete results in continuing microstructural changes (e.g., slow hydration, crystallization of amorphous constituents, and reactions between cement paste and aggregates). Therefore, it is important that changes over long periods of time are measured, monitored, and analyzed to best support long-term operations and maintenance decisions.

Structural health monitoring (SHM) is required to produce actionable information regarding structural integrity that, when conveyed to the decision-maker, enables risk management with respect to structural integrity and performance. The methods and technologies employed include assessment of critical measurements, monitoring, and analysis of aging concrete structures under different operating conditions. In addition to the specific system being monitored, information may also be available for similar or nominally identical systems in a fleet, as well as legacy systems. Therefore, Christensen (1990) suggested that assessment and management of aging concrete structures in NPPs requires a more systematic approach than simple reliance on existing code margins of safety.

Through the Light Water Reactor Sustainability Program, several national laboratories and Vanderbilt University have begun research on concrete SHM in accordance with the proposed framework discussed Section 1.1. The goal of this research is to enable plant operators to make risk-informed decisions on structural integrity, remaining useful life, and performance of concrete structures across the nuclear fleet. The long-term research objective of this project is to produce actionable information regarding structural integrity that supports operational and maintenance decision making, which is individualized for a given structure and its performance goals. In addition, the project supports the research objectives of three pathways under the Light Water Reactor Sustainability Program (i.e., the Advanced Information, Instrumentation, and Control Systems Technologies Pathway, the Materials Aging and Degradation Pathway, and the Risk-Informed Safety Margin Characterization Pathway).

This report presents a demonstration example performed at Vanderbilt University using various techniques to assess ASR degradation in controlled concrete specimens. The demonstration example showcases the effectiveness of the proposed concrete SHM framework. A summary of the initial research findings and future research activities are also presented in this report.

1.1 Background

Vanderbilt University, in collaboration with Idaho National Laboratory and Oak Ridge National Laboratory personnel, is developing a framework for health diagnosis and prognosis of aging concrete structures in NPPs that are subject to physical, chemical, and mechanical degradation (Mahadevan et al. 2014; Agarwal and Mahadevan 2014). The proposed framework (shown in Figure 1) will investigate concrete structure degradation by integrating the following four technical elements:

(1) monitoring, (2) data analytics, (3) uncertainty quantification, and (4) prognosis. For details on each element of the proposed framework, refer to Mahadevan et al. (2014). The framework will enable plant operators to make risk-informed decisions on structural integrity, remaining useful life, and performance of the concrete structure.

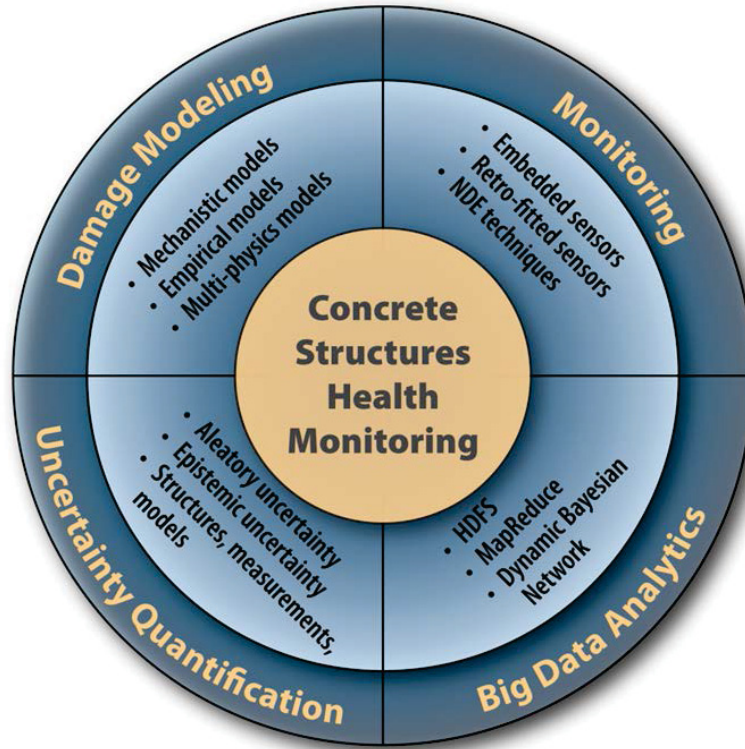


Figure 1. Elements of concrete structural health monitoring.

1.1.1 Monitoring

This element explores an effective combination of promising SHM techniques for full-field multi-physics monitoring of concrete structures. Optical, thermal, acoustic, and radiation-based techniques are being investigated for full-field imaging. Examples of these techniques include digital image correlation (DIC), infrared imaging, velocimetry, ultrasonic, and x-ray tomography. A particular consideration is the linkage of chemical degradation mechanisms to the observed degradation, which requires synergy between monitoring and prognosis.

1.1.2 Data Analytics

Information gathered from multiple health monitoring techniques results in a high volume, rate, and variety (i.e., heterogeneity) of data. This element leverages big data techniques to store, process, and analyze heterogeneous data (i.e., numerical, text, and image) and arrive at effective inference of concrete degradation. The data analytics framework can also integrate information from model prediction, laboratory experiments, plant experience and inspections, and expert opinion. Data mining, classification and clustering, feature extraction and selection, and fault signature analyses with heterogeneous data can be orchestrated through a Bayesian network for effective inference.

1.1.3 Uncertainty Quantification

This element quantifies the uncertainty in health diagnosis and prognosis in a manner that facilitates risk-management decisions. Sources of natural variability, data uncertainty, and model uncertainty arising in both modeling and monitoring activities can be considered and their effects quantified. In addition to

measurement and processing errors, data uncertainty due to sparse and imprecise data for some quantities and due to large data on other quantities (i.e., data quality, relevance, and scrubbing) can be considered. Model uncertainty in multi-physics degradation modeling due to model form assumptions, unknown model parameters, and solution approximation errors can be included. Various uncertainty sources do not combine in a simple manner, and the Bayesian network offers a systematic approach for comprehensive uncertainty quantification in a manner that is informative to the decision-maker for operation, maintenance, inspection, and other risk-management activities.

1.1.4 Prognosis

This element leverages modeling of chemical, physical, and mechanical degradation mechanisms (such as alkali-aggregate reaction, chloride penetration, sulfate attack, carbonation, freeze-thaw cycles, shrinkage, and radiation damage) in order to assist monitoring and risk management decisions. Alkali-aggregate reaction is currently receiving prominent attention; however, other appropriate damage mechanisms for NPP concrete structures can be included. This element leverages modeling and computational advances and combined-physics experiments and integrates multiple models through an appropriate simulation framework. This combined model can be used for a prognosis of damage based on the present state of damage obtained from the diagnosis result. The uncertainty quantification in the diagnosis can be propagated through the prognosis model to quantify uncertainty in the prognosis.

1.2 Report Layout

The objective of this report is to demonstrate how the four elements of concrete SHM for ASR degradation can be connected, using a simple demonstration example. Section 2 discusses preparation of specimens with ASR degradation and laboratory experimental set up for the various monitoring techniques. Data analysis of the collected monitoring data is presented in Section 3. Section 4 provides integration of all data analytics results to perform uncertainty quantification. The MapReduce technique for handling big data is also demonstrated. In Section 5, the prognosis of future ASR growth using a finite element analysis and an ASR gel expansion model is presented. A research summary and future activities are discussed in Section 7.

2. EXPERIMENTAL STUDY

This research investigates the monitoring of physical-chemical-mechanical coupled degradation in concrete via full-field imaging techniques (i.e., thermal, optical, and vibrational). Effective combinations of full-field techniques need to be identified for different types of concrete structures under different loading and operating conditions. In this report, monitoring techniques implemented include infrared imaging, DIC, mechanical deformation measurements, nonlinear impact resonance acoustic spectroscopy (NIRAS), and vibro-acoustic modulation (VAM). The monitoring techniques are studied with concrete samples constructed and cured in the laboratory. The concrete samples are described in the next subsection.

2.1 Sample Preparation and Curing

ASR is a slow-developing process that can take several decades to come to fruition. In the laboratory, aggressive conditions are applied to accelerate this process. Using sodium hydroxide (NaOH) in the mix water or placing the cured concrete in an NaOH solution causes an increase in pH. Selecting highly reactive siliceous aggregates or glass will provide an available source of silica. Lastly, curing the specimens at higher temperatures (i.e., 60°C to 80°C) will accelerate ASR. Using these three factors, ASR gel can be produced in the laboratory within several months.

2.1.1 Cement Bricks

In the first batch of bricks, six cement samples were cast, with dimensions of $9 \times 5 \times 2$ in. Glass was placed in the six bricks as shown in Figure 2, where the shaded regions represent slices of glass.

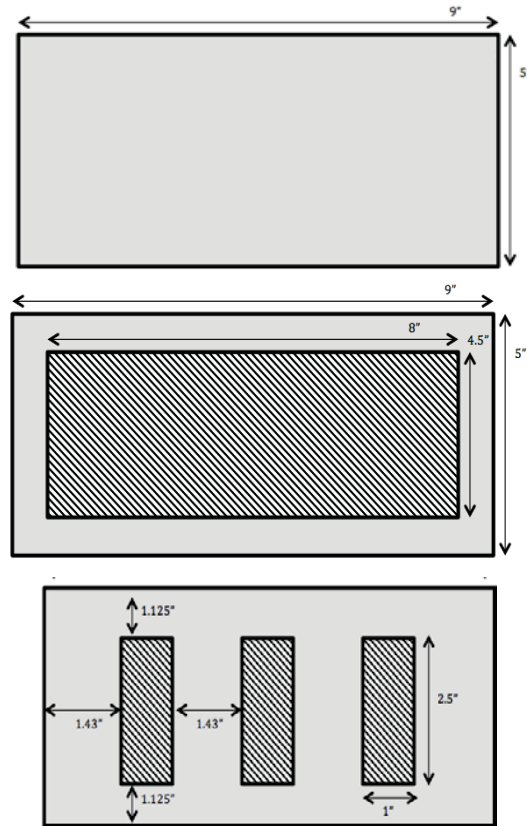


Figure 2. Sketches of A1/A2 (top), B1/B2 (middle), and C1/C2 (bottom), where the shaded region represents glass slices.

Figure 3 shows Sample B2 after 2 months of aggressive curing. Cracking and a whitish effluent is noticed.



Figure 3. Brick B2 showing whitish effluent (ASR gel).

After the first batch of specimens, reusable plexiglass molds were created. In the second batch of six bricks, aggregates were placed in pockets inside the bricks as they were cast. The aggregates were placed in pockets to control the location where ASR would occur. A sketch of the aggregates is shown in Figure 4 and Figure 5 shows brick Number 6 during casting.

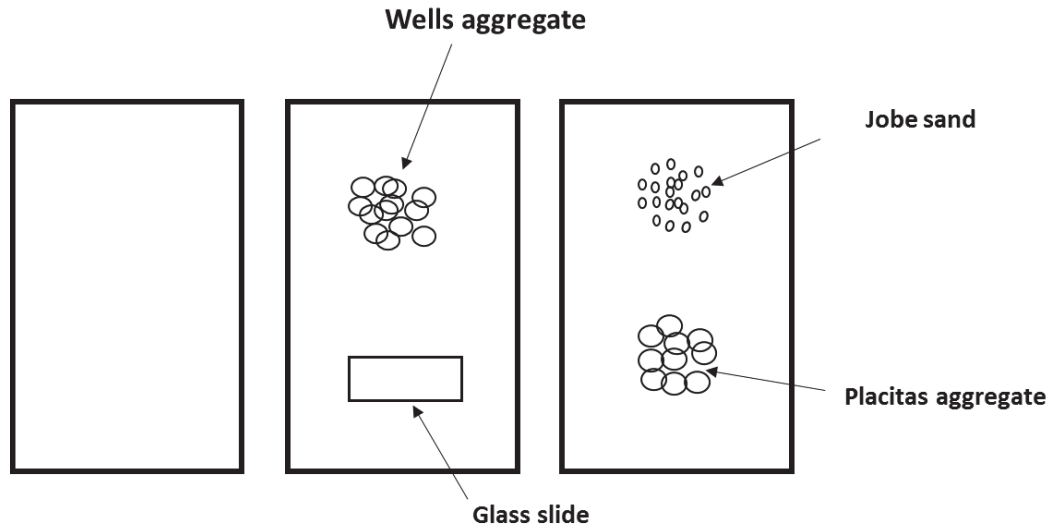


Figure 4. Aggregate type and location in the second batch of samples.



Figure 5. Brick Number 6 during casting of the second batch of samples.

In order to accommodate mechanical deformation measurements (discussed later), 1-1/2-in. stainless steel pegs were inserted into several of the samples when they were cast. Stainless steel is nonreactive in sodium hydroxide. The pegs can be seen during casting in Figure 6.



Figure 6. Stainless steel pegs being inserted during casting.

2.1.2 Cement Slab

The goal of the small brick samples discussed above was to accelerate the occurrence of ASR and use the slabs for non-destructive testing. While much can be gained from studying these small samples, scaling up the size of the concrete samples will further yield valuable information. With the ultimate objective being detection of ASR in real-world structures, it is necessary that a larger slab be constructed that more accurately imitates what is seen at NPPs. This larger slab was cast in December 2015 and has dimensions of 2 ft \times 2 ft \times 6 in. Figure 7 shows an image of the slab immediately after the mold was removed.



Figure 7. 2-ft \times 2-ft \times 6-in. cement slab.

A slab of this size presents challenges in material required for casting, space for curing, maneuverability for non-destructive testing, transportation from the casting location to testing facility, and for detecting ASR.

2.1.2.1 Pockets of Aggregate. Four types of aggregate are placed in pockets at a depth of 3 in. in four quadrants of the slab. The aggregates are placed in pockets instead of being dispersed throughout the slab; therefore, the reactivity of each aggregate can be determined independently. Additionally, because the locations of the pockets of aggregate are known, this information can be used to validate localization of ASR from non-destructive testing. The four types of aggregates used are as follows:

- Silica – powder from a local ceramic shop
- Wells – coarse aggregate from Wells, Maine, provided by Dr. Eric Giannini at the University of Alabama
- Placitas – coarse aggregate from Placitas, New Mexico, provided by Dr. Eric Giannini
- Spratt – coarse aggregate from Spratt quarry in Ontario, Canada, provided by the Ontario Ministry of Transportation.

The pockets of aggregate are labeled in Figure 8. All of these aggregates are known to be highly reactive.

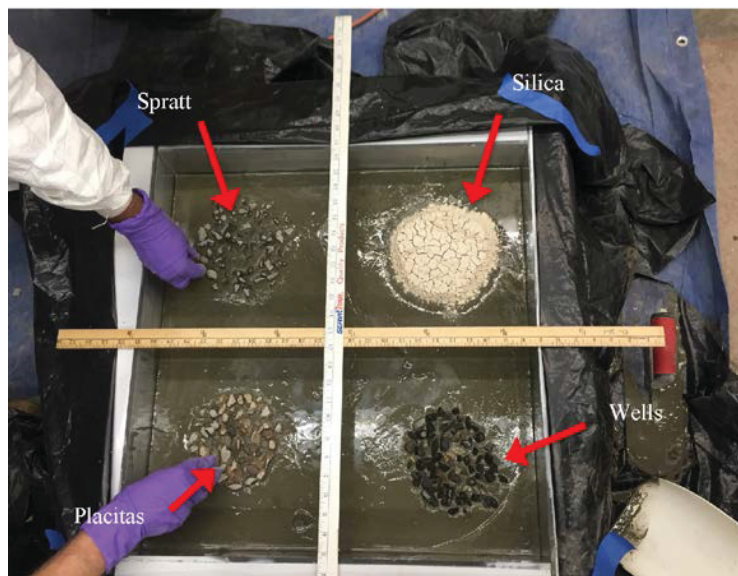


Figure 8. Pockets of aggregate labeled in a cement slab during pouring.

Significant effort was spent preparing the infrastructure necessary to support, transport, and cure the slab. Personnel included two staff engineers, two graduate students, and the principal investigator; the setup is designed to support casting, transportation, and curing of multiple slabs. The essential elements of the setup are briefly described in the following subsections.

2.1.2.2 Reusable Mold. The mold for the slabs is made of plexiglass. Plexiglass also was used for the brick specimens; it produces a smooth surface and can be easily removed after the slab has hardened. The sides of the mold are supported by aluminum channels that are screwed together and attached with stainless steel brackets. This allows the mold to be easily disassembled and reassembled. The bottom is supported by several sheets of plywood and has runners underneath in order to facilitate lifting from the bottom by a forklift. The completed mold prior to casting is shown in Figure 9.

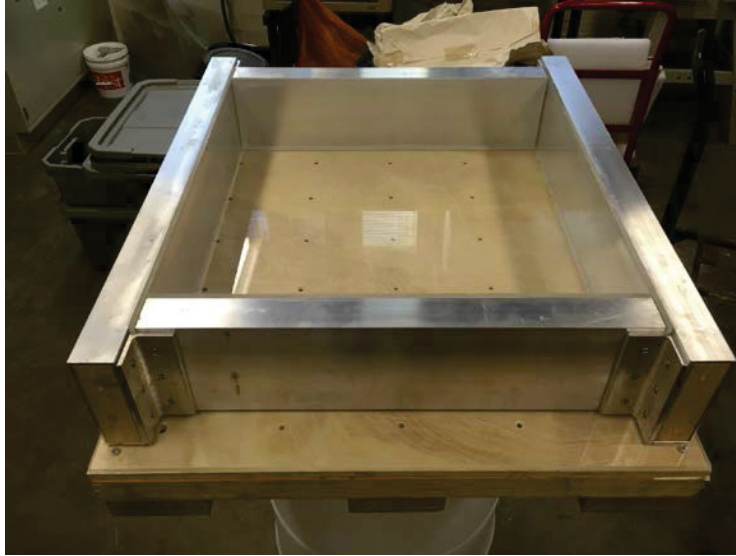


Figure 9. 2-ft \times 2-ft \times 6-in. mold.

2.1.2.3 Curing Tub. A stainless steel piece of sheet metal is bent and welded along the seams to form a watertight tub with four sides. This tub is used for curing the slab. Figure 10 shows the slab being lowered into the tub by a crane located in the casting facility. The slab is resting on the frame. The chains are attached to rods that are threaded into the connections on the frame. The wooden plank simply acts as a spacer, keeping the chains from collapsing inward and crushing the slab. Inside the tub, metal spacers are used to keep the slab at a height above water level during the curing process.



Figure 10. Slab sitting on the frame being lowered into the tub.

The slab is placed in the tub 1 day after it is cast, giving it time to harden. The tub is also used when the slab undergoes accelerated curing in the oven at the Laboratory for Systems Integrity and Reliability. A forklift is used to lift the slab into the oven (Figure 11). The slab is cured above water at 60°C.



Figure 11. Slab being placed in the oven for accelerated curing.

2.2 Non-Destructive Examination Techniques

2.2.1 Infrared Thermography

Infrared thermography maps the thermal load path in a material. In the case of concrete, cracking, spalling, and delamination all create a discontinuity in the thermal load path. Additionally, rebar and tensioning cables can be easily detected due to the difference in thermal conductivity coefficients between steel and concrete. Thermography has even been shown to detect debonding between the reinforcing steel and concrete. Infrared thermography can be either an active or passive monitoring technique. When heat is locally added to the structure to create a temperature gradient, it is referred to as active. If the solar heat is used to provide heat to produce the temperature gradient, it is considered passive. Passive infrared thermography is preferred because it is less energy intensive. The Electric Power Research Institute showed the feasibility of infrared thermography by mapping a 450,000-ft² dam. During the 2 days that the Electric Power Research Institute spent mapping the dam, numerous potential delamination sites were identified (Renshaw et al. 2014). Kobayashi and Banthia (2011) combined induction heating with infrared thermography to detect corrosion in reinforced concrete. Induction heating uses electromagnetic induction to produce an increase in temperature in the rebar. When corrosion is present, it inhibits the diffusion of heat from the rebar to the surrounding concrete. Infrared thermography is then used to capture the temperature gradient. It was concluded that the temperature rise in corroded rebar is higher than in non-corroded rebar, a more-corroded rebar yields a smaller temperature rise on the surface, and the technique is more effective with larger bar diameters and smaller cover depths (Kobayashi and Banthia 2011). The current study is investigating the performance of infrared thermography as a means of identifying ASR.

2.2.2 Digital Image Correlation

Digital image correlation is an optical non-destructive examination technique that is capable of measuring the deformation, displacement, and strain of a structure (Bruck et al. 2012). During NPP routine pressure tests on containment vessels, when the internal pressure reaches 60 psi, it might be possible to use DIC to determine deformation of the concrete containment. DIC is capable of detecting surface defects such as cracks, micro-cracks, and spalling, but is unable to detect any subsurface defects. The primary benefit of DIC is in measuring deformation; therefore, its ability to detect changes in the dimensions of the slab due to ASR gel expansion is of interest in this study. DIC requires a speckled pattern on the specimen

to anchor observations at different time instants. This also presents a problem for the small brick specimens that are immersed in NaOH solution or water; the pattern is disturbed and partly dissolved in the NaOH solution. However, the slab specimen in Figures 10 and 11 is cured above water; therefore, DIC might be applicable.

2.2.3 Mechanical Deformation Measurement

The mechanical deformation measurement is a contact measurement technique. Calipers or an extensometer can be used to measure deformation along a linear distance. It is often convenient to glue on targets or cast nails into the concrete to provide more repeatable measurement points. In order to capture the ASR-induced concrete deformation, the measurement device needs to be accurate to within a few hundred microns. Most high-resolution mechanical measurement devices have a relatively short measuring span (i.e., 1 foot or less). This makes them ideal for laboratory experiments, but limits their applicability in real-world structures without using a significant number of targets glued to the structure.

2.2.4 Non-Linear Impact Resonance Acoustic Spectroscopy

NIRAS is a non-destructive testing technique that uses the vibrational response of a structure to classify damage. It was developed at Georgia Tech to detect ASR-induced damage in concrete (Lesnicki et al. 2014). NIRAS operates based on the following idea: a linear system has the same natural frequency regardless of the amplitude of the excitation force; this is not true for nonlinear systems. In a nonlinear system, the resonant frequency will shift depending on the amplitude of the excitation force. Because ASR causes micro-cracking within the concrete, which creates nonlinearity, it is believed that NIRAS can be used to detect damage in concrete before the cracking is visible on the surface. Because NIRAS is a global vibrational response technique (i.e., it measures shifts in resonant frequency), it is better suited for small laboratory concrete specimens than large concrete structures. For example, if a large concrete structure had a small patch of ASR growth, it is unlikely that NIRAS would be able to detect it is because it will have a minimal effect on the natural frequency of the structure.

2.2.5 Vibro-Acoustic Modulation

VAM is vibrational-based non-destructive testing that has been successful in detecting nonlinearities in various materials (Kim et al. 2014), but has not been used for concrete. We investigated the potential of using VAM in ASR detection of concrete bricks. VAM works by simultaneously exciting a structure with two frequencies of vibration. The low-frequency input is termed the “pump” and the high-frequency input is termed the “probe” (Kim et al. 2014). Interaction of the pumping and probing signals indicates the presence of nonlinearities in the system. Figure 12 shows a simple beam with a crack.

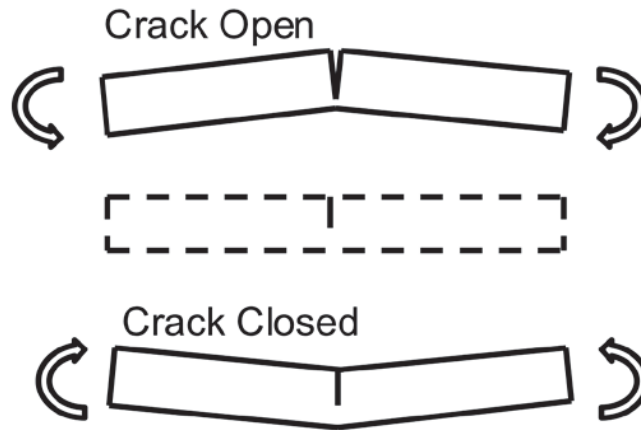


Figure 12. VAM representation of system response to pumping signal.

As the pumping signal causes the crack to open and close, the effective cross-sectional area the probing signal can travel through changes. Thus, the amplitude of the probing signal is transmitted through the beam changes with the phase of the pumping signal. This modulation will produce side bands around the probing frequency (Figure 13).

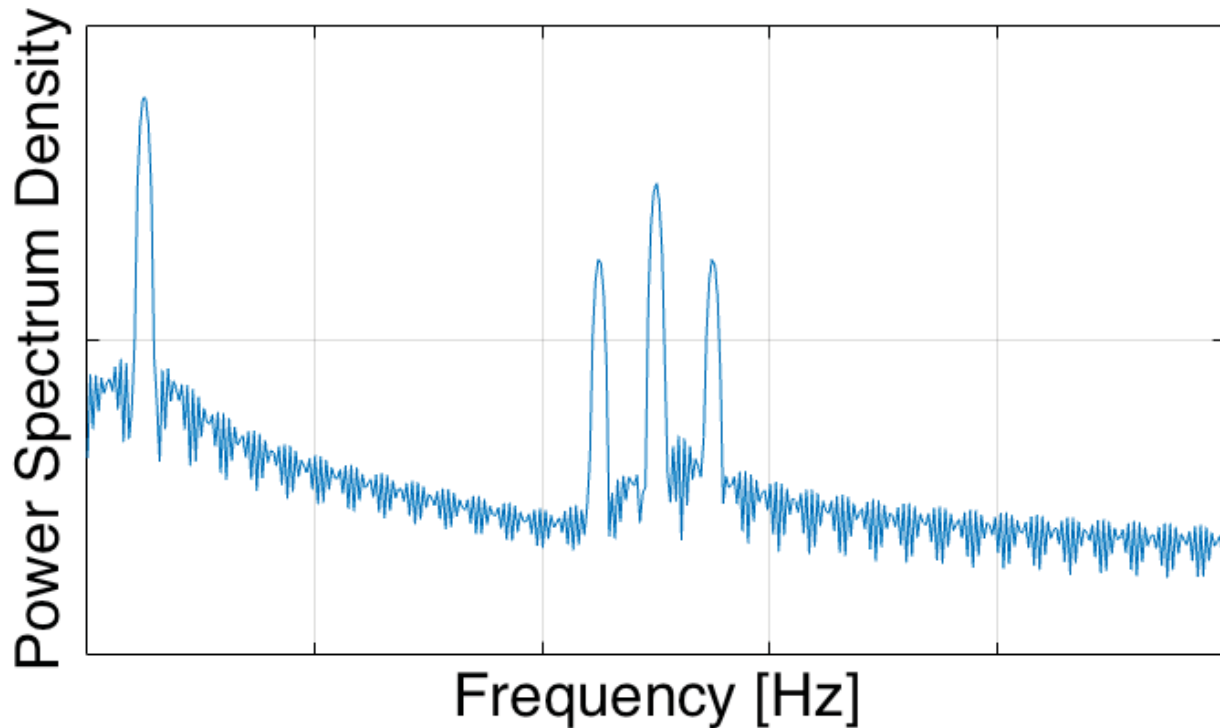


Figure 13. Side bands indicating modulation.

2.3 Non-Destructive Examination Experimental Setup

2.3.1 Infrared Thermography Experimental Setup

For thermography imaging, a FLIR® infrared (IR) camera was used to detect the temperature contours on the surface of the concrete slab. These contours were analyzed to detect flaws or defects in the slabs that cannot be easily detected by visual inspection. The IR camera has a resolution of 512×640 pixels, which is a high number for an IR camera, and is placed on a stand approximately 10-ft tall to capture an image of the entire concrete specimen. The concrete specimen is placed on a thermal heating blanket. In addition, the HEATCON® composite system controller was connected to the thermal blanket and used to program a defined thermal cycle that can be repeated as many times as needed for a test. A thermocouple was placed between the thermal blanket and the concrete sample to measure and monitor the heat applied by thermal blanket. For the concrete bricks, the scaled heating cycle is given in Figure 14. Figure 15 shows the thermal blanket during testing of three of the bricks. The bricks were tested in groups of three to save time. Because the slab has significantly more mass than the bricks, a longer heating cycle was required to raise the temperature (Figure 16).

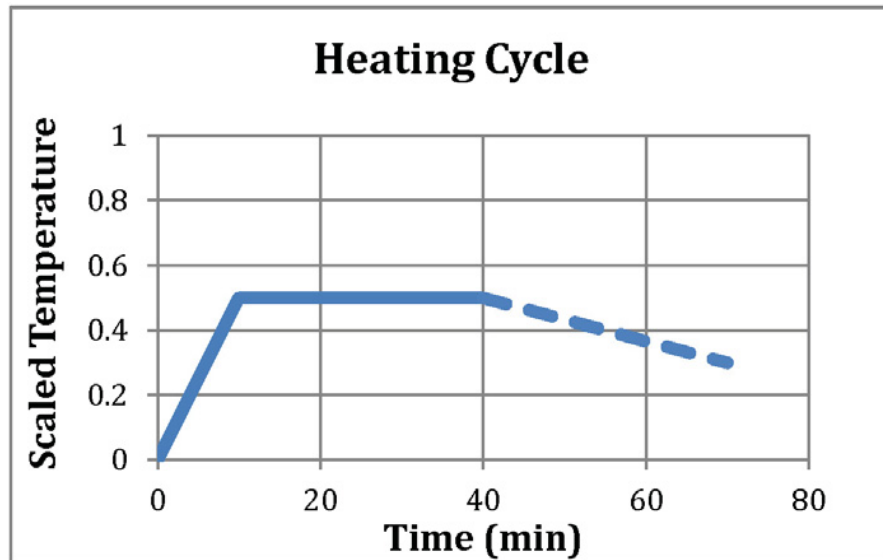


Figure 14. The heating blanket's temperature cycle for the bricks.



Figure 15. Small bricks on the thermal heating blanket.

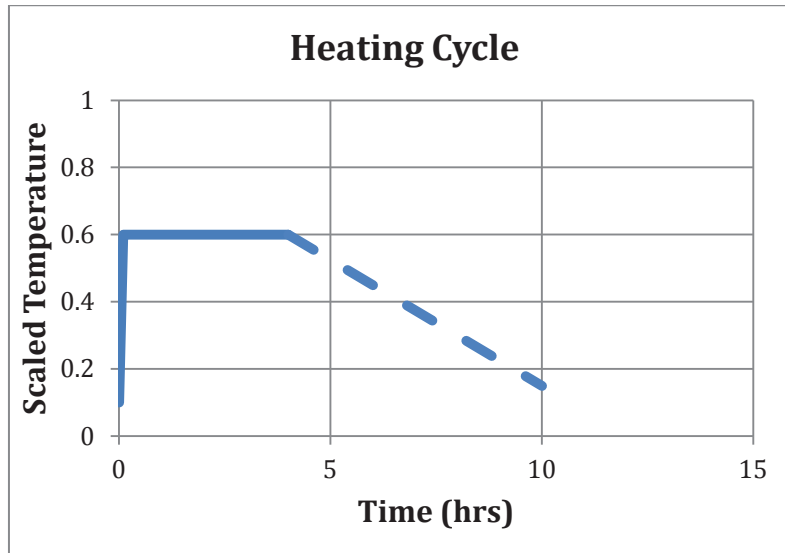


Figure 16. The heating blanket's temperature cycle for the slab.

2.3.2 Digital Image Correlation Setup

Two high-resolution cameras on a specialized stand and a software package comprise the DIC equipment. Before testing, an extensive calibration process is required to inform the software where the cameras are in space relative to the concrete samples. This guarantees that deformation measurements in all three dimensions will be accurate. The samples also must be prepared before testing. The concrete samples were covered in a speckled pattern; therefore, deformation could be detected through DIC. The speckled pattern was made by painting the specimens black and using a white spray paint to create the randomly placed speckles. A brick with the speckled pattern is shown in Figure 17. DIC calculates deformation by taking a baseline image and comparing all subsequent images to the baseline. Each image is broken up into square facets and the program identifies movement in these facets between images. From an experimental standpoint, it is important to realize that there are always ambient vibrations that will affect data. We found that our noise floor, due to ambient vibrations when calculating deformation, was around 1 to 2 microns. Figure 18 shows output from the DIC software. The team found a limitation in the DIC software – each time a sample was moved between images (e.g., because it was returned to the oven for continued curing), the software would recalculate the facets. This made it impossible to compare images if the sample had been moved. This also makes it impossible to test more than one sample at a time. The team is currently looking into ways to solve this limitation.



Figure 17. Brick with speckled pattern.

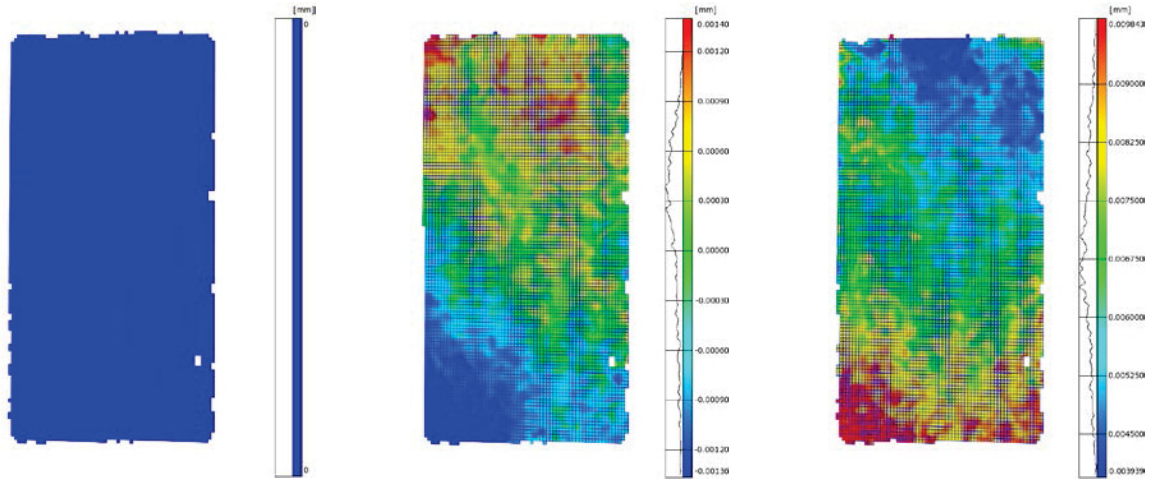


Figure 18. Results from DIC.

2.3.3 Mechanical Deformation Measurements

Calipers are used to take length measurements; comparison of these measurements overtime reveals whether any deformation has occurred. The calipers shown in Figure 19 have a maximum length of 1 ft and a resolution of 0.001 in.



Figure 19. Calipers used for mechanical deformation measurements.

Steel nails were cast into the concrete samples in order to provide a point for taking measurements. Figure 20 shows the nails being used in taking a measurement.



Figure 20. Measuring the distance between nails on a brick.

2.3.4 Set Up of Non-Linear Impact Resonance Acoustic Spectroscopy

Impact from a modal hammer is used to excite the samples over a broadband frequency range. We impact the sample on the top surface at the same location for each hit. The location is arbitrary, but avoiding major lines of symmetry improves the response. An accelerometer is used to measure the sample's vibrational response. Accelerometers are also placed on the top surface, avoiding all lines of symmetry; however, their locations are not trivial. Because we are interested in capturing the first natural frequency of the samples, the accelerometers need to be placed at the ends of the concrete bricks because their first mode shape is bending in the long direction. Figure 21 shows the location of impact and measurement.



Figure 21. NIRAS test setup.

The bricks are placed on a foam mat, because this represents an unconstrained condition and allows for reduced noise in the data. Both the impact force from the hammer and the vibrational response from the accelerometers are sent to a data acquisition system, where they can be output into MATLAB for further analysis. The vibration response of one of the bricks is shown in Figure 22.

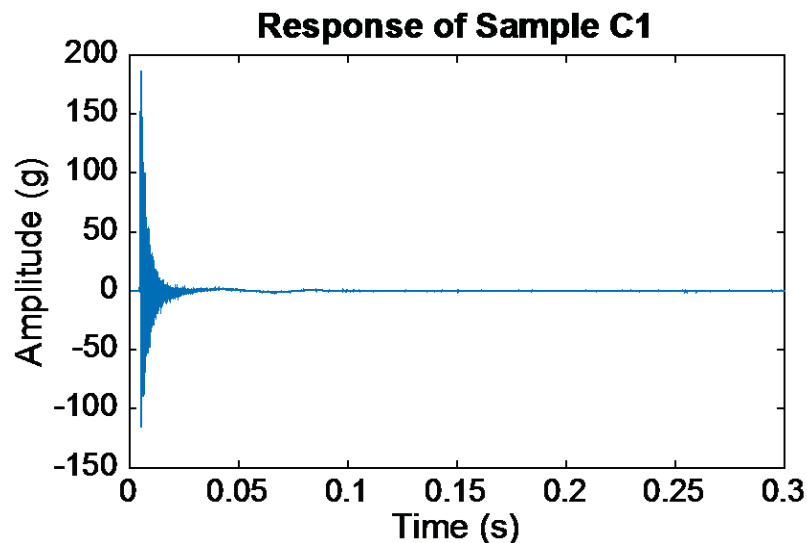


Figure 22. Raw acceleration data from NIRAS.

2.3.5 Vibro-Acoustic Modulation Setup

The concrete bricks are placed in a simply supported condition for this test. The modal hammer strikes the bricks to create an impulsive load that is used as the low frequency “pump.” A piezo-stack actuator acts as the high frequency “probe.” A triaxial accelerometer measures the sample’s response. A sampling frequency of 51.2 kHz facilitates the high-frequency probe, and a sampling period of 0.1 s resolves modulated side bands. Variance impact forces and probing frequency are evaluated. Optimal pumping and probing frequencies are system dependent; however, in general, a higher probing-to-pumping ratio is preferred.

3. DATA ANALYTICS

3.1 Alkali-Silica Reaction Detection in Brick Samples Using Infrared Thermography

The study of small brick samples is reported here. Six samples were used for this study as shown in Figure 2 earlier (i.e., A1/A2 – plain cement; B1/B2 – brick containing a glass plate almost throughout; and C1/C2 – brick containing three glass slides). The suffixes 1 and 2 indicate curing in water at room temperature versus curing in NaOH at 80°C).

The hypothesis is that formation of ASR should change the heat conductivity within the slab. Therefore, there would be a temperature difference between the water-cured and NaOH-cured slabs at each time stamp. The temperature difference between the water-cured data and NaOH-cured data for Slab A at each time stamp is selected to be the baseline temperature difference. The corresponding temperature differences for Slab B and Slab C are expected to be different from the baseline. Based on the baseline Slab A, upper bound and lower bound values (at each time instant) are selected for the temperature difference between water-cured data and NaOH-cured data. If the temperature difference is outside the bounds, then a change in heat conductivity is indicated, implying the formation of ASR. To set boundaries, maximum and minimum values of the temperature difference were selected among all pixels between the water-cured data and NaOH-cured data for Slab A at each time stamp. The results of this analysis are shown in Figure 23, indicating that the entire area of Slab B2 has ASR and parts of Slab C2 have ASR.

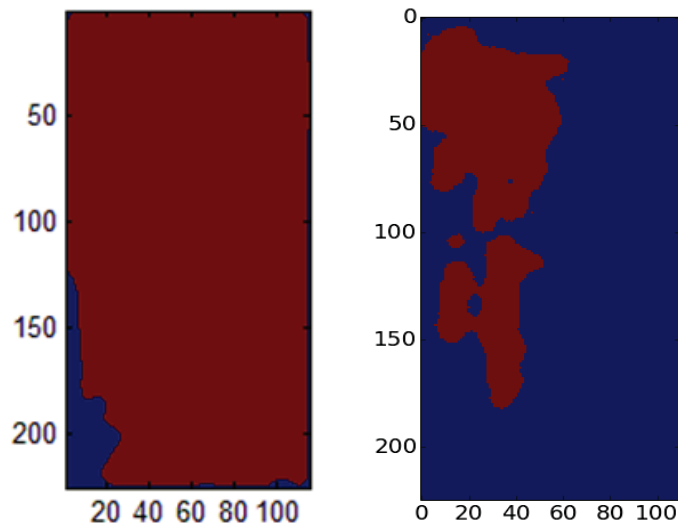


Figure 23. Slab B2 (left) and Slab C2 (right). ASR is indicated by the red areas.

3.2 Detection Using Nonlinear Impact Resonance Acoustic Spectroscopy

Raw acceleration data are converted from the time domain to the frequency domain using the fast Fourier transform in MATLAB. From the frequency domain, the first resonant frequency will be identified. A shift in resonance frequency of a concrete sample for increasing force input amplitudes will be detected, which indicates the system is nonlinear (i.e., there is micro-cracking due to ASR).

The nonlinearity parameter quantifies the severity of damage. It is calculated by simply finding the scaled slope of the input force amplitude versus the frequency shift. It has been observed that concrete samples with more severe damage will generally have a larger value for the nonlinearity parameter. If a sample is in pristine condition, it should have no frequency shift with increasing input force amplitude, thus a nonlinearity parameter value of 0. Figure 24 and Figure 25 show NIRAS results for one of the small bricks that has reactive aggregate and was cured in NaOH. Even though there is no sign of damage on the surface of the block, NIRAS was able to detect nonlinearity.

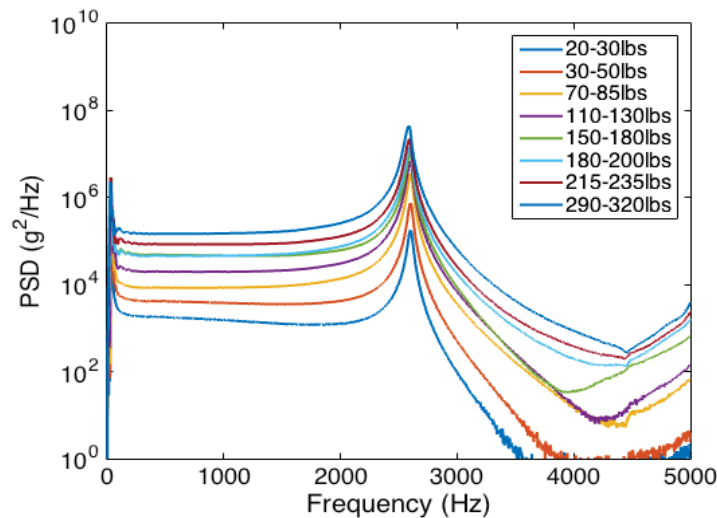


Figure 24. Results from a concrete brick, showing frequency shift with increasing input force amplitude.

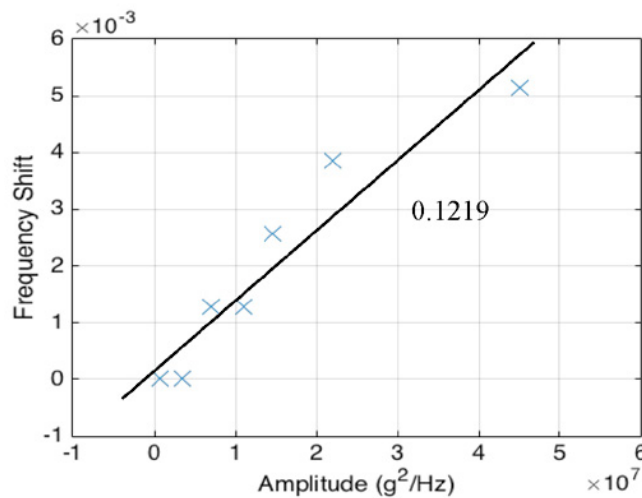


Figure 25. Calculation of nonlinearity parameter for the brick specimen.

NIRAS was also performed on the large slab. It was impacted in each of its four quadrants. Results from this test are shown in Figure 26 and Figure 27.

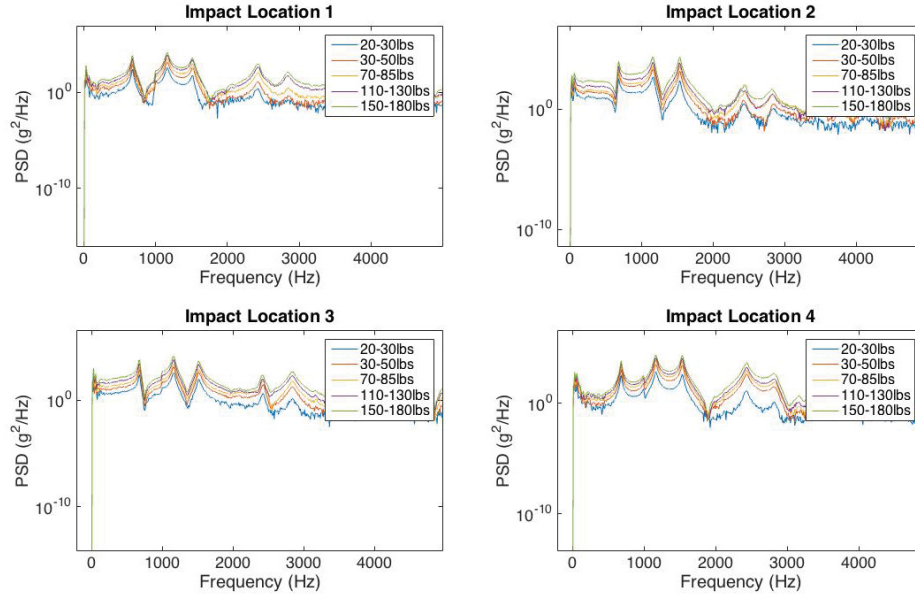


Figure 26. Frequency response of the large slab to impact excitation in four locations.

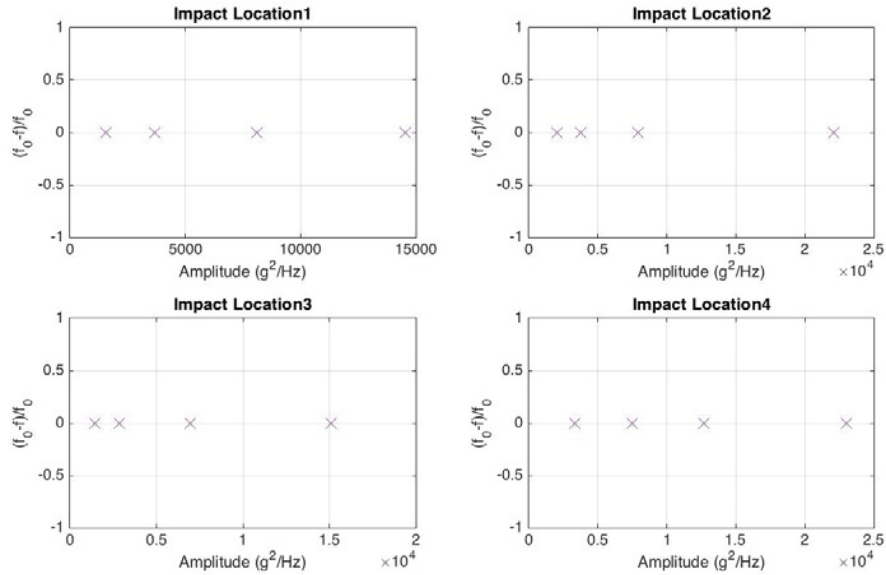


Figure 27. Resonant frequency shift of the large to increasing impact force.

From the results, it is clear that no damage was detected in the slab after 2 months of accelerated curing. There are several possible reasons for this, including the following:

- There is no damage in the slab.
- Impact force is not large enough because a small modal hammer was used when a modal sledge hammer may be more appropriate
- There were the limitations of NIRAS in scaling up to large structures.

3.3 Vibro-Acoustic Modulation

Similar to NIRAS, the resonant frequency is determined in this technique as well. However, in VAM, the data are inspected for modulation about the probing frequency. It is this modulation that indicates nonlinearity within the system. VAM results for the brick samples (i.e., A2, B2, and C2) are shown in Figure 28. Several potential damage indices based on spectrum properties were considered as follows:

- Ratio of side band amplitude to probe or pump amplitude
- Ratio of side band bandwidth power to probe or pumping power (integral under power spectral density)
- Percent of total power present in side band power.

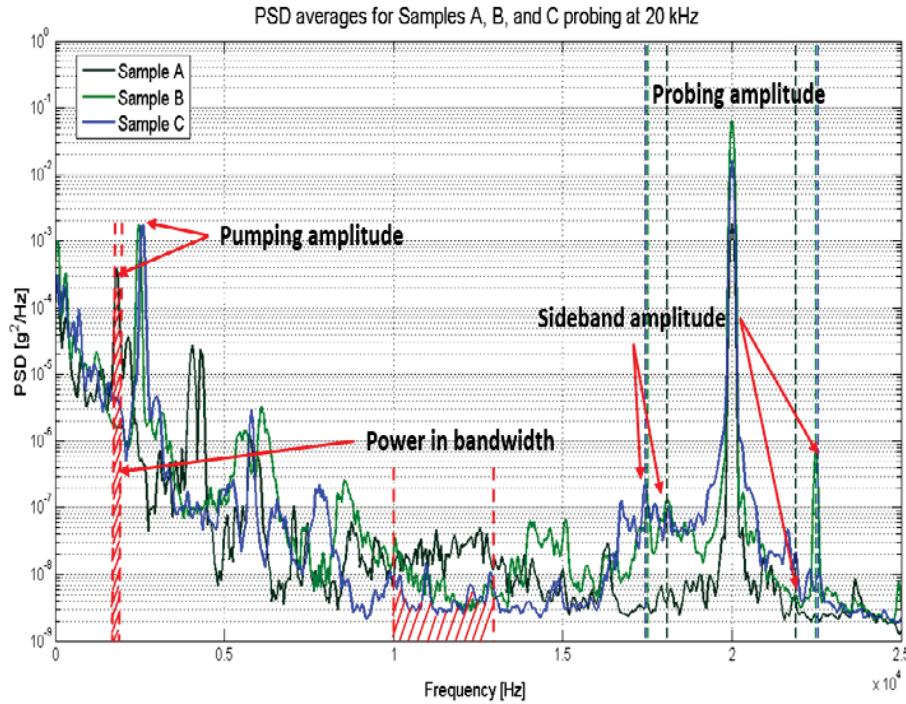


Figure 28. VAM results for three concrete bricks.

From the VAM results above, a damage index was calculated. For comparison, NIRAS was also performed on these samples.

Strong correlation between the VAM damage index and the NIRAS nonlinearity parameter that is given in Table 1 indicates there is good promise in using VAM for ASR detection in concrete.

Table 1. Comparison of VAM and NIRAS results.

Sample	Resonant Frequency	Probing Frequency	Pumping Power Ratio	VAM Damage Index (Normalized to A)	NIRAS Nonlinearity Parameter
A2	1,900 Hz	20 kHz	0.0000575	1.00	0.00
B2	2,450 Hz	20 kHz	0.0004819	8.38	1.6929
C2	2,550 Hz	20 kHz	0.000166853	2.90	0.1219

4. DIAGNOSIS

4.1 Diagnosis

4.1.1 Data Fusion

Because multiple non-destructive examination techniques are exercised above, fusion of data from multiple techniques can provide more accurate and reliable information when compared to information from each individual technique. Based on the abstraction levels of the available data, there are three types of data fusion techniques: (1) pixel level, (2) feature (or characteristic) level, and (3) decision level (Castanedo 2013; Hall and Llinas 1997; Kokar and Kim 1993).

4.1.1.1 Pixel Fusion. When data obtained from multiple sensors are commensurate, data can be fused in a pixel level. For non-destructive testing data fusion, different combination methods can be applied in the pixel level (Gros et al. 1999) such as maximum amplitude, integration, and weighted averaging. Bayesian methods can also be used. Because pixel level fusion is only valid for homogeneous data, it is more commonly applied in image processing.

4.1.1.2 Feature Fusion. Different features extracted from the raw data can be fused and decisions can be made based on the joint feature vector. There are different feature fusion techniques such as neural network and Kalman filter. Sometimes the effective fusion part is essentially only concentration of vectors.

An example of applying a Kalman filter in the detection of ASR in concrete bar has been reported (Quadri and Sidek 2014; Lu et al. 2009; Liu et al. 2001) using multiple sensors. Acoustic, electromechanical, optical, and embedded sensors were used to sample data. First, different features for different sensors were extracted. To integrate the heterogeneous features, a decentralized Kalman filter was applied on the transferred binary data (i.e., positive/negative and high/low). The outcome was a set of best features, without redundancy. Then a neural network was trained, with the selected features as inputs and expansion as output.

4.1.1.3 Decision Fusion. Decision fusion operates at the level of decision, after obtaining individual diagnosis results from each technique. Several popular decision fusion methods available in structural health monitoring are voting, Bayesian method, fuzzy logic, and Dempster-Shafer theory. One example of a voting method for decision fusion has been reported with ultrasonic structural health monitoring via multi-sensor. Four transducers were installed on the specimen and six combinations of feature-transducer pairs were formed. Six features (such as normalized mean squared error, drop in correlation coefficient, and differential curve length) were sampled. Based on the selected thresholds (i.e., different for each different feature and transducer pair), each feature voted “damaged” or undamaged. A simple majority vote was used for the overall decision.

4.1.1.4 Bayesian Network. This study applies a Bayesian network for decision-level fusion, because it can also be used for uncertainty quantification. Bayesian networks are directed, acyclic, graphical representations with nodes to represent the random variables and arcs to show the conditional dependencies among the nodes. Each arc is associated with a conditional probability relation between the parent and child node. In this study, results from three monitoring techniques are merged: (1) IR, NIRAS, and VAM. Data obtained from IR are images, while data acquired from NIRAS and VAM are signals. Because we are performing decision-level fusion, diagnosis results from the techniques will be used instead of raw data. NIRAS and VAM detect ASR by evaluating the nonlinearity of the structure, which are global methods; while analysis of IR indicates the actual area of ASR. The NIRAS and VAM results are used to update the Bayesian network, followed by updating the IR results. **Damage** is a binary variable, which indicates whether the structure has ASR or not. A_{true} is the ASR area, whose parent node is **Damage**. When **Damage** is 0, A_{true} is also 0 with probability 1; when **Damage** is 1, a probability distribution is assumed for the ASR area. **A** is a variable representing the ASR area detected by IR, which

is formed by adding an observation error variable to the true area. C_1 and C_2 are two categorical variables that represent the ASR detection by NIRAS and VAM. Similar to A , there might be observation error terms added to them (Figure 29). All priors and conditional probability functions need to be determined or assumed according to the analyst's knowledge of the sample and devices.

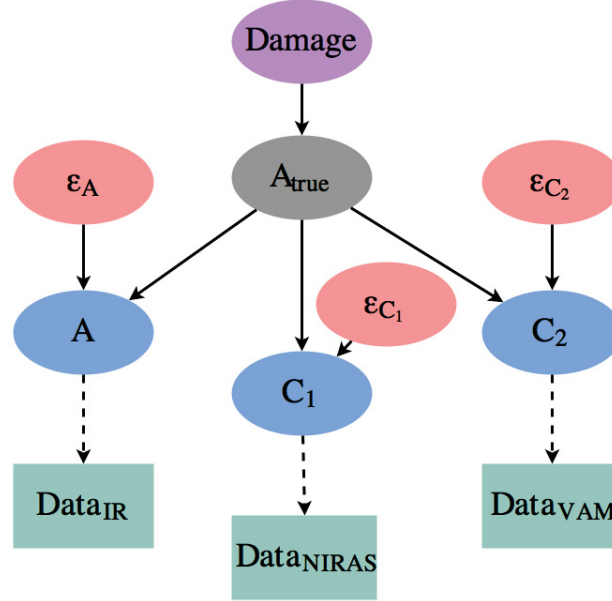


Figure 29. Bayesian network for data fusion of IR, NIRAS, and VAM.

4.1.2 Results

A binomial distribution is assumed as the prior of the binary indicator variable *Damage*, while a uniform distribution is assumed for damage size A_{true} when $Damage = 1$. The observation error of IR is assumed as Gaussian distribution, while for the sake of simplicity, there is no observation error for NIRAS and VAM. C_1 and C_2 are assumed as binomial distributions. Notice that the parameter P is defined as a step function to account for the false alarm ($A_{true} = 0$) probability and sensing accuracy ($2 \geq A_{true} > 0$ and $A_{true} > 2$) (Figure 30).

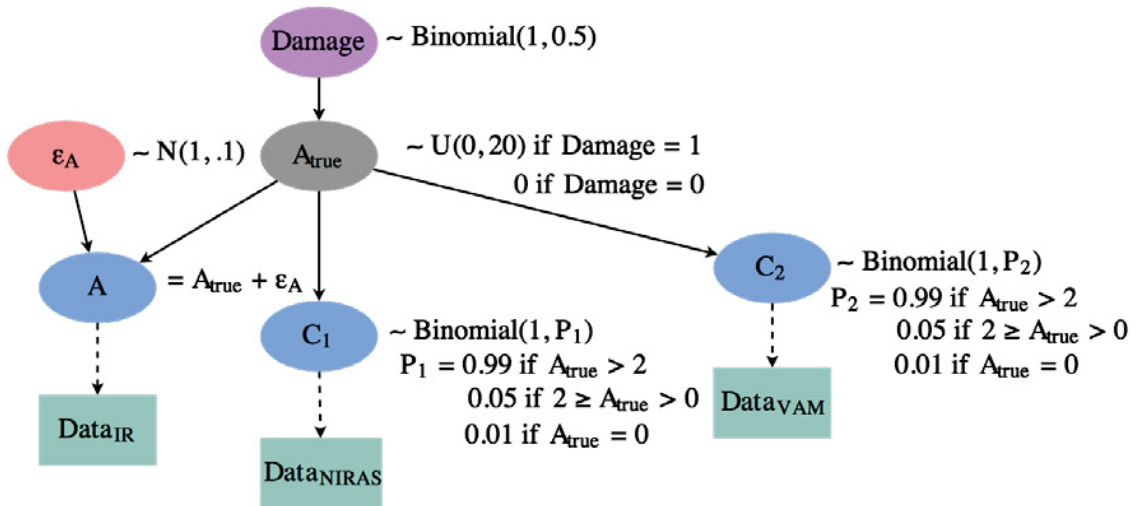


Figure 30. Bayesian network being used.

As explained previously, the network will be updated first by the decisions (results from data analysis) of NIRAS and VAM and then by IR results. In the context of the Bayesian network, the results from the data analysis are treated like observations. Here we have three observations, one each from NIRAS, VAM, and IR (see Table 2).

Table 2. Observations.

Sensor	Value	Unit
NIRAS	True	—
VAM	True	—
IR	10.545	in^2

After updating by NIRAS and VAM, the probability of damage increased from 50 to 98.84% (Figure 31). Uncertainty regarding the damage area is also narrowed from the uniform distribution (Figure 32). After observation of IR, the damaged area's uncertainty is further updated to be a normal distribution, with a mean of $9.99 in^2$, and standard deviation of $0.99 in^2$ (Figure 32).

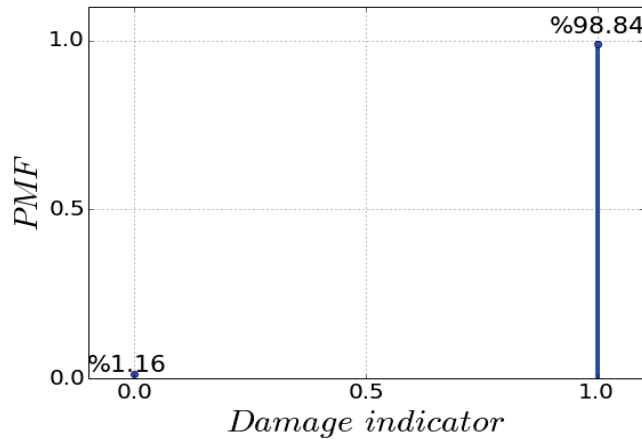


Figure 31. Updated damage indicator.

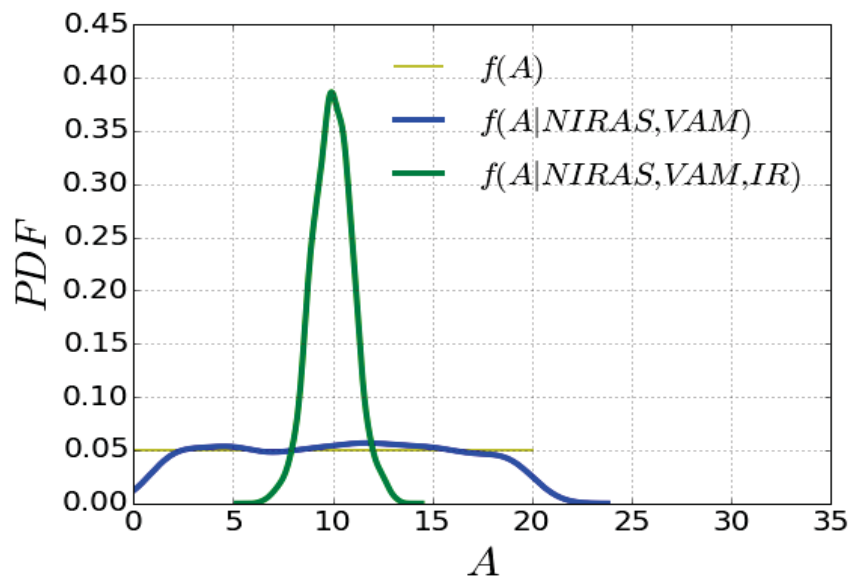


Figure 32. Damage area updated by NIRAS, VAM, and IR.

4.2 Big Data Analytics

The above example problem took less than 1 minute to complete the Bayesian updating calculation using Markov Chain Monte Carlo (MCMC) sampling. However, under continuous online monitoring of real structures, the Bayesian network can become large (with multiple possible damage locations) and the number of observations will become very large. Although the data size of decision results to be fused is not large, it still qualifies as a big data problem, because MCMC sampling is expensive. Therefore, the MapReduce technique is implemented in this section with a view toward realistic applications.

4.2.1 MapReduce

MapReduce is a framework designed for large datasets, which utilizes multiple nodes (i.e., machines) for computations (Dean and Ghemawat 2008). MapReduce takes key/value pairs as input and generates the other key/value pairs as outputs. As indicated literally, the MapReduce framework can be split into two steps: map and reduce, both of which are created by the user. Before applying the MapReduce model, the user will need to write the input as the key/value pair. The key/value pair ($k1, v1$) will then be fed into the map function, which will generate the intermediate key/value pairs ($k2, v2$). Then the intermediate key/value pairs are passed to the reduce function, which merges together these values to form a possibly smaller set of values. The process is shown below, which allows us to handle lists that are too large to fit into the memory:

map ($k1, v1$) \rightarrow list ($k2, v2$)

reduce ($k2, \text{list}(v2)$) \rightarrow list ($v3$).

To implement this framework, a cluster of computers are called nodes. One of them is called the master node and the rest are slave nodes. As shown in Figure 33, the master node is in charge of communicating with the user program and assigning the tasks to the slave nodes (i.e., workers). First, the input files are parsed and split into many pieces (with sizes of 16 to 64MB). The master will identify the idle workers and assign each with a map task or reduce task. Then each worker will do its own task and when all tasks are completed, the output files will be obtained.

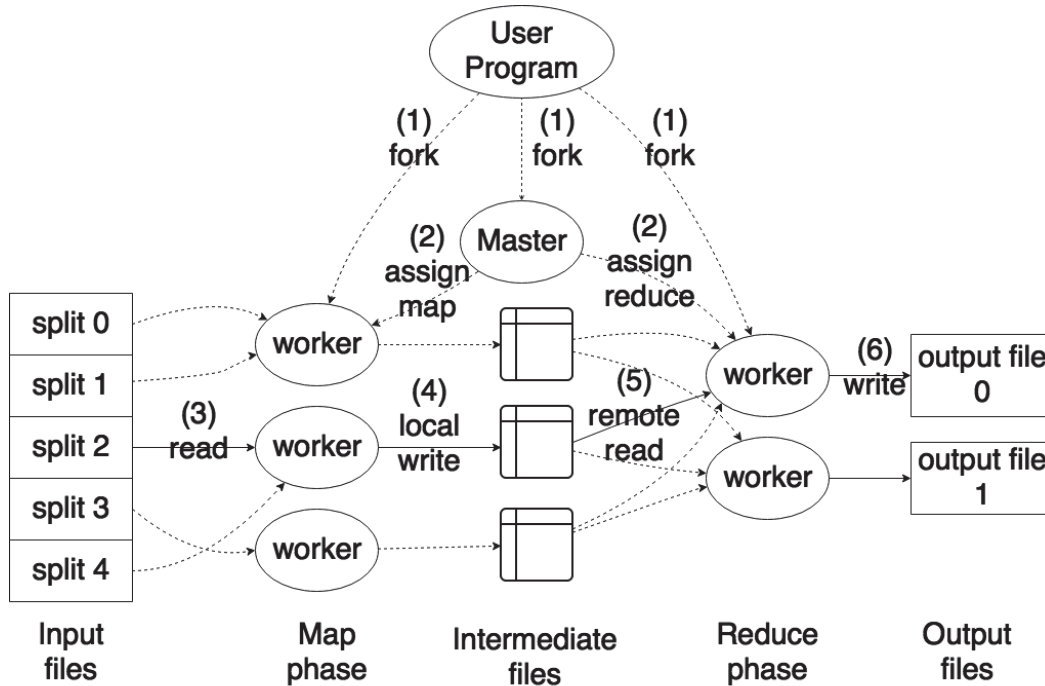


Figure 33. MapReduce execution overview.

4.2.2 Parallelization of Markov Chain Monte Carlo

The basic idea of the MCMC parallelization (Neiswanger et al., 2013) is to divide observations into M splits and each node takes one partition to update the network. The prior of the variable of interest will be updating using the equation:

$$p_m(\theta) \propto p(\theta)^{1/M} p(x^{n_m}|\theta) \quad (21)$$

After all nodes complete their task, all subposterior samples from each node will be combined to produce samples for an estimate of the subposterior density product $p_1 \dots p_M$, which is proportional to the full data posterior, i.e., $p_1 \dots p_M(\theta) \propto p(\theta|x^N)$.

4.2.3 Results

Synthetic data are used here to illustrate the above procedure. The data are generated by sampling from $N(10, 1)$, with a data size of 10,000. Only five computing nodes are used for the sake of illustration. It is found that the efficiency is quite high (Figure 34), without losing accuracy (Figure 35). Notice that because the computation time is almost linearly proportional to the data size, the efficiency is stable for MCMC parallelization.

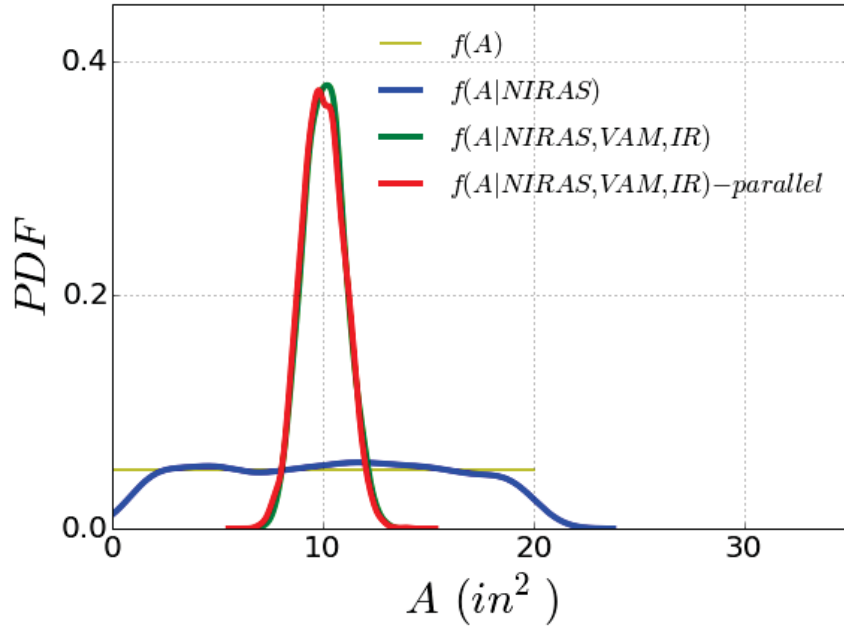


Figure 34. Accuracy of parallelization.

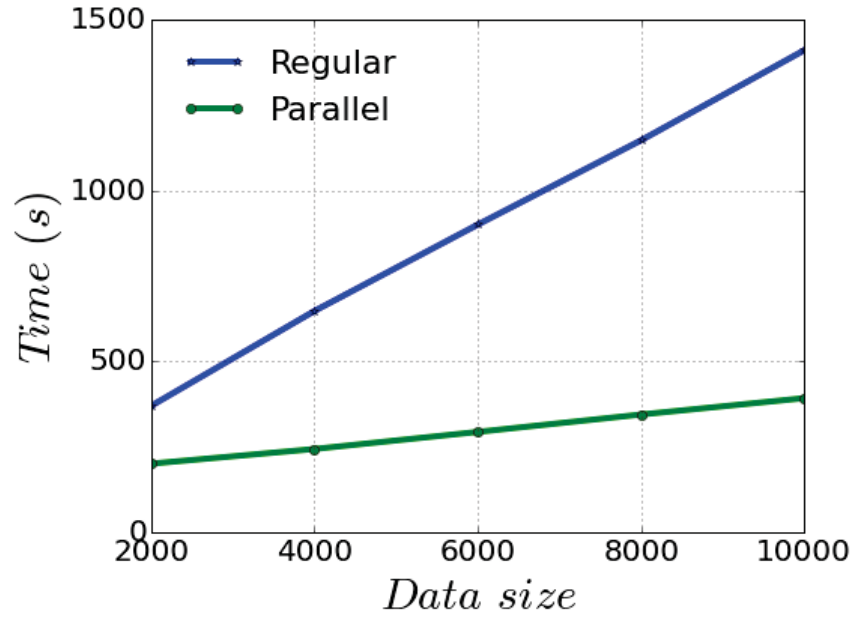


Figure 35. Efficiency of parallelization.

5. PROGNOSIS

5.1 Alkali-Silica Reaction Finite Element Model

After diagnosis is carried out via the Bayesian network, we are able to do the prognosis, based on the calibrated ASR area. A finite element model is needed to predict the behavior of the structure in the future. We have implemented the ASR expansion model developed by Saouma and Perotti (2006) in Abaqus.

5.1.1 Implementation of Saouma and Perotti's Model

ASR can first be attributed to a hydrophilic gel due to complex dissolution-precipitation reactions between reactive silica in aggregates. Then, in the presence of water in the pores, the gel expands, creating an increasing internal pressure in localized regions within the cementitious structure, causing initiation of microscopic or even macroscopic cracks. There are two main factors that control the ASR reaction rate: (1) temperature, the higher the temperature, the faster ASR occurs and grows (Ulm et al. 2000). This kinetic effect of temperature on ASR results from the thermos-activation of the dissolution of reactive silica on aggregate-cement interface and the precipitation of gel. (2) Humidity: water plays an important solvent role for silica dissolution, intervenes as transport media for diffusion of ions through pore network, and is a necessary compound for the formation of various reaction products (gels and other mineral precipitates). Therefore, accurate predictions of the effects of ASR on long-term performance and response of aged concrete structures require a fully coupled thermo-hydro-mechanical-chemical model. Among many ASR-related models developed over the past few decades, a thermodynamically consistent coupled thermo-chemo-mechanics model of ASR was developed by Ulm et al. (2000), based on an extensive experimental study by Larive (1997). However, it does not include the effect of stress-state on the reaction kinetics and volumetric swelling. Farage et al. (2004) further extended Ulm's model by including a smeared cracking approach to model cracking of concrete due to ASR expansion. However, only heat conduction was considered and the moisture diffusion was not considered in these coupled thermo-chemical-mechanics models. One more serious limitation of this ASR swelling model is that the swelling strain is treated isotropically without stress dependency. Saouma and Perotti (2006) presented a comprehensive coupled thermo-hydro-mechanical-chemical model for ASR based on Ulm's model, and

considered the effects of stress on the reaction kinetics and anisotropic volumetric expansion induced by ASR. The following effects are included in Saouma and Perotti's model:

1. ASR expansion strain is treated as a full strain tensor, instead of being calculated separately and independently for each principal direction.
2. ASR reaction rate is temperature dependent and relative humidity is also crucial.
3. ASR reaction can be retarded by compressive stress within concrete structures.
4. ASR expansion is redistributed into other less-constrained principal directions.
5. Both high compressive or tensile stress states inhibit ASR expansion due to the formation of micro and macro-cracks that absorb the expanding gel.
6. A triaxial compressive stress state reduces expansion.
7. ASR reaction extent will lead to a reduction in both tensile strength and elastic modulus.

This model is implemented in this report, with Abaqus finite element analysis. Although during the diagnosis, the ASR area was detected with uncertainty quantified, we only illustrate the prognosis use of the damaged area here (Figure 36). The prognosis model is demonstrated with the C2 brick. The dimensions of the specimen are 9 x 5 x 2 in., with all four sides unconstrained. The 3,520 (= 11 x 20 x 16) elements were used in the finite element model (Figure 37). All material parameters and ASR-related parameters are listed in Table 3.

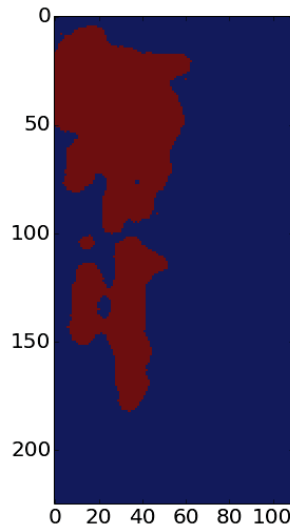


Figure 36. ASR detection in C2 (red: ASR).

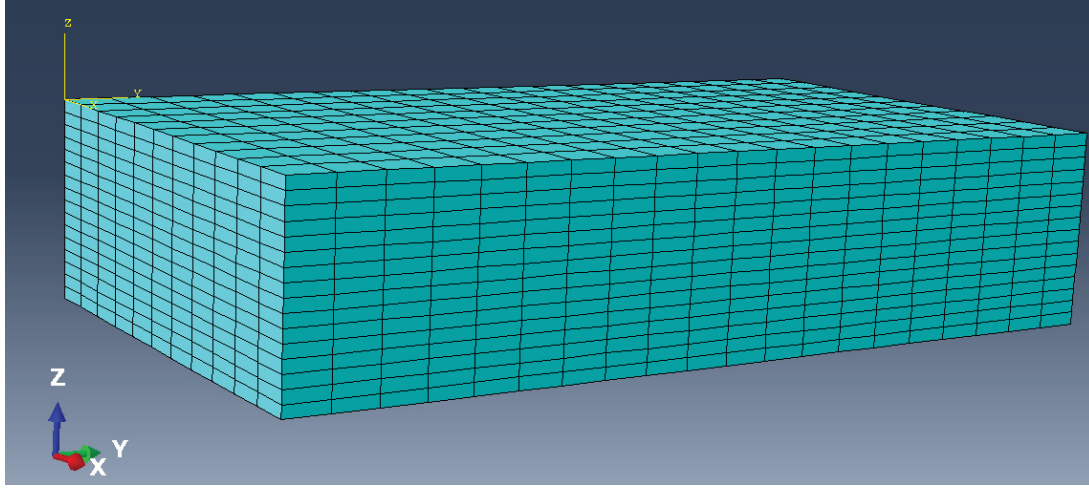


Figure 37. Finite element mesh of C2 brick.

Table 3. General parameters of the ASR model.

Characteristics	Symbol	Unit	Value
Maximum volumetric ASR strain at test temperature T_0^{test}	ε^∞	—	0.00262
Characteristic time at test temperature T_0^{test}	τ_C	day	68.9
Latency time at test temperature T_0^{test}	τ_L	day	110.0
Activation energy associated with τ_C	U_C	K	5,400
Activation energy associated with τ_L	U_L	K	9,400
Residual reduction factor	Γ_r	—	0.5
Tensile strength	\dot{f}_t	MPa	3.2
Residual reduction factor for ASR expansion under tensile stress	γ_r	—	0.5
Fraction of \dot{f}_t prior to reduction of ASR expansion due to macro-cracking	γ_t	—	0.5
Compressive strength	\dot{f}_c	MPa	— 31
Upper compressive stress beyond which there is no more ASR expansion	σ_u	MPa	— 8
Concrete Young's modulus	E_0	GPa	37.3
Concrete Poisson's ratio	ν	—	0.22
Reduction fraction for Young's Modulus at end of ASR reaction	β_E	—	0.5
Reduction fraction for tensile strength at end of ASR reaction	β_f	—	0.5

The basic idea is to map the ASR detection results by assigning ASR extent (ξ) to be 1 for the element in the corresponding location. To be more realistic, a linearly decrease of ξ for the neighboring elements are assigned, with an interval of 0.25. The assigning plan is shown schematically in Figure 38. The glass is known in the middle of the brick, with an average thickness of 1/16 in. Therefore, the mentioned ASR extent assigning pattern is applied to elements in the middle layer of the model (in the z direction).

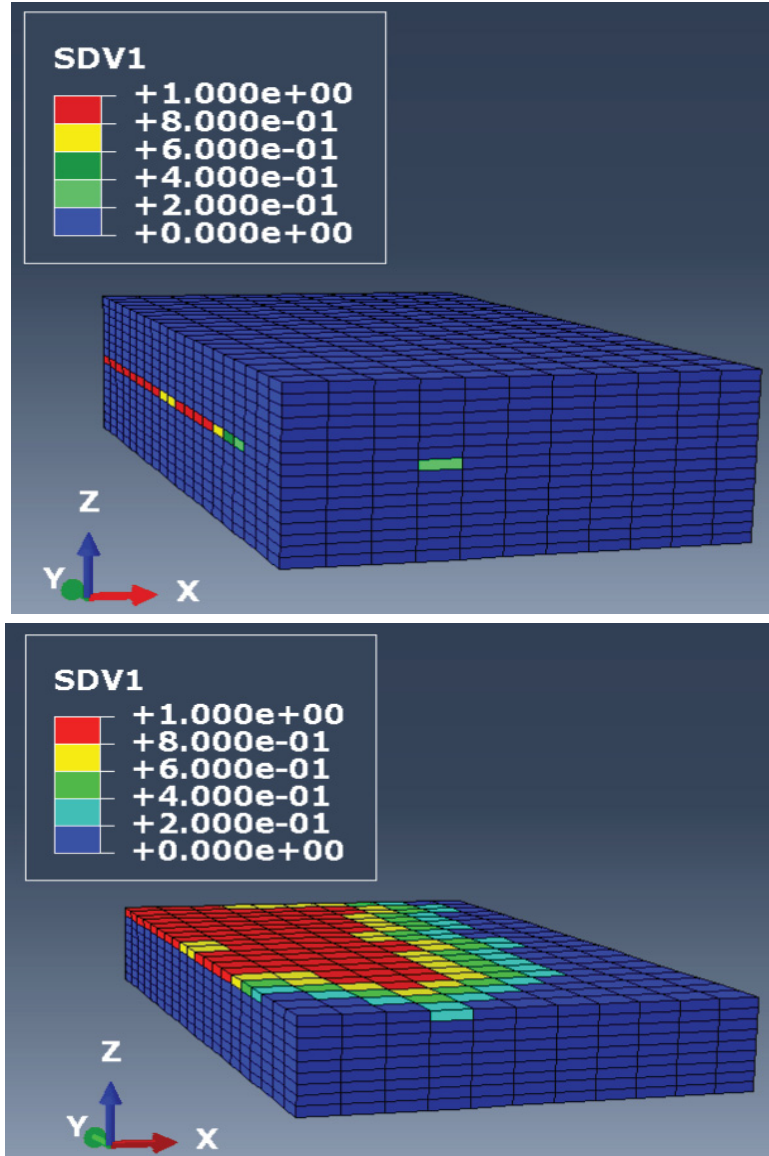
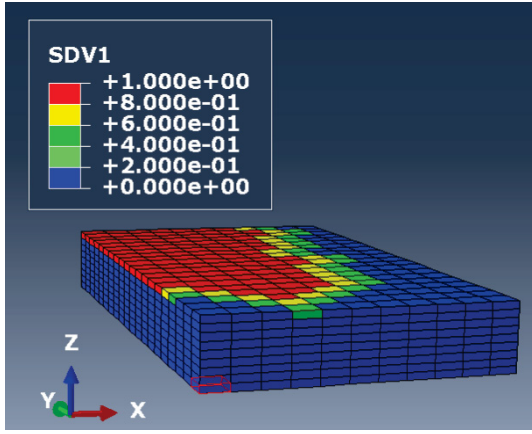
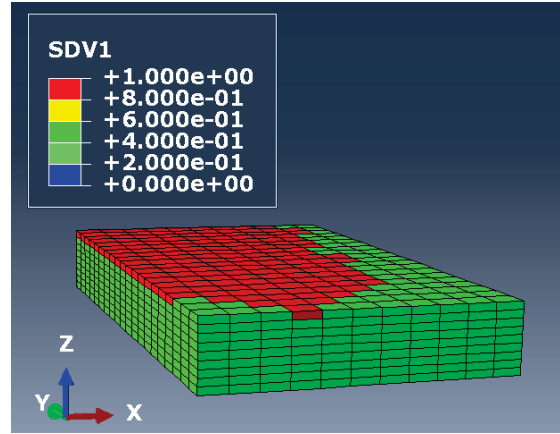


Figure 38. Model initial condition for prognosis (above: full model view; below: cut view).

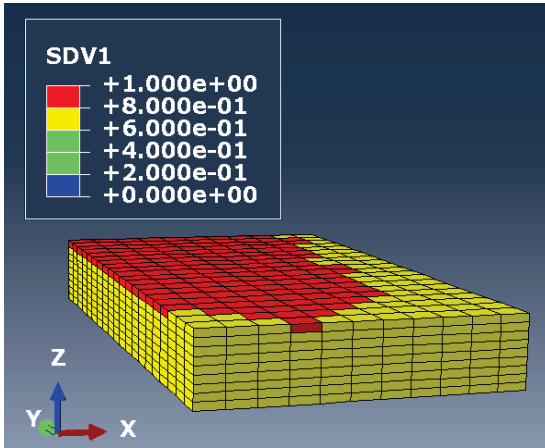
Based on the initial conditions shown in Figure 38, the future ASR extent is predicted by simulation. The status of the specimen at four future time instants (i.e., $t = 60 \text{ days}$, $t = 120 \text{ days}$, $t = 180 \text{ days}$, and $t = 240 \text{ days}$) are shown in Figure 39. It can be easily observed that ASR is growing along time. Also notice that at $t = 240 \text{ days}$, the entire structure is highly developed with ASR ($\xi > 0.8$). Figure 40 shows the time history of ASR growth for the selected element (highlighted in Figure 39 (a)).



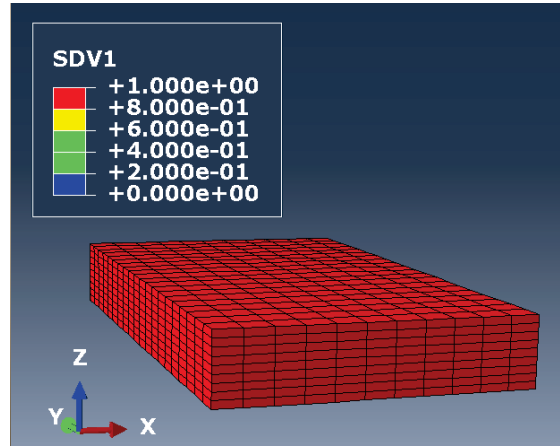
(a) ASR extent @ t = 60 days



(b) ASR extent @ t = 120 days



(c) ASR extent @ t = 180 days



(d) ASR extent @ t = 240 days

Figure 39. Future prediction of ASR growth (half model).

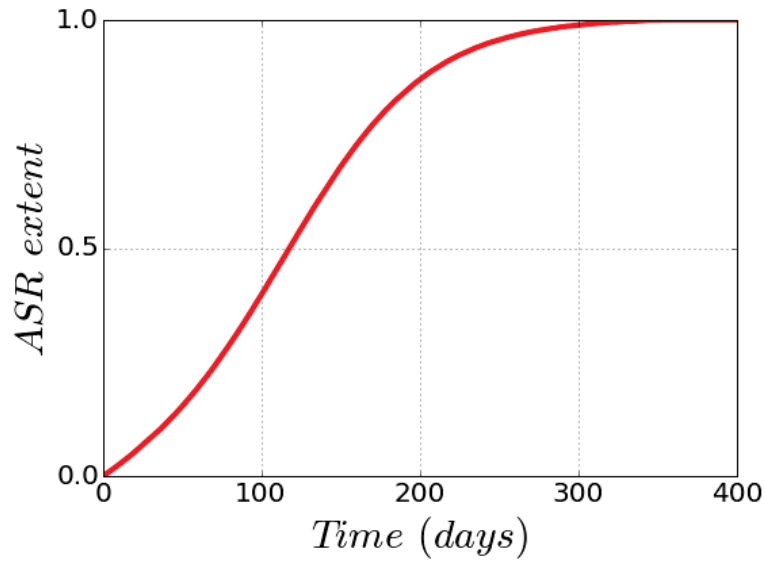


Figure 40. Time history of ASR extent.

6. SUMMARY AND FUTURE WORK

This report presented a simple demonstration problem to illustrate the integration of four elements of the proposed SHM framework for ASR degradation monitoring of concrete structures. The demonstration problem considered small cement specimens without and with ASR degradation and possible techniques in each of the four elements of the framework and their integration. Effective combinations of monitoring techniques, data analytics, and diagnosis/prognosis were illustrated.

1. Experimental study:

- Specimens of two sizes were cast to develop accelerated ASR degradation: (1) small bricks ($9 \times 5 \times 2$ in.) and (2) medium slab ($24 \times 24 \times 6$ in.)
- Various siliceous materials (such as glass, silica powder, and reactive aggregates) were used to prepare different sets of samples; an NaOH solution was used in the concrete mix or in the curing solution to raise the pH level
- DIC and mechanical deformation measurements using calipers were used to measure changes in the dimensions of the specimens
- IR, NIRAS, and VAM techniques were used to diagnose the damage.

2. Data analytics:

- Themographic images of the specimens collected using the FLIR® IR camera, vibration data from NIRAS, and VAM were analyzed to diagnose ASR degradation
- The diagnosis results were then used as inputs for the Bayesian network and prognosis model.

3. Uncertainty quantification and big data implementation:

- Information from multiple techniques were fused using a Bayesian network
- Uncertainties in the damage area were quantified
- A MapReduce technique for handling big data was demonstrated with synthetic data.

4. Prognosis:

- A coupled thermo-hydro-mechanical-chemical model for ASR degradation has been implemented in Abaqus through a user subroutine (UMAT)
- Prognosis of ASR degradation is performed based on the current state of degradation obtained from diagnosis.

Future work will focus on the following tasks during the next year:

1. Preparation of a slab specimens with reinforcement and subjected to aggressive curing to produce ASR.
2. Study of smaller brick specimens with different control conditions to isolate the most critical component responsible for rapid growth of ASR gel.
3. Refinement of non-destructive examination techniques for larger specimens and specimens with reinforcement.
4. Localization and quantification of the damage and exploration of embedded sensors (e.g., pressure, temperature, strain, and chemical).

5. Application of a dynamic Bayesian network approach to diagnosis and prognosis to track evolution over time.
6. Fusion of heterogeneous data in the presence of large amounts of observation data and use of MapReduce for dynamic Bayesian network parallelization.
7. Refinement of the prognosis model to account for reinforcement (contact problem is a challenge), smeared crack (convergence could be a problem), moisture, and heat transfer in a more realistic way.
8. Application of the diagnosis/prognosis framework to other small samples available at the University of Alabama.
9. Coordination with ongoing research activities at the University of Tennessee, Knoxville and Oak Ridge National Laboratory to construct and monitor a large mock-up. In particular, explore the application of DIC.
10. Overall, this research focuses on data analysis and development of uncertainty-quantified diagnostic and prognostics models that will support continuous assessment of concrete performance. The resulting comprehensive approach will facilitate development of a quantitative, risk-informed framework that could be generalized for a variety of concrete structures and could be adapted for other passive structures. Future work will investigate the methods illustrated in this report to realistic structures and damage scenarios.

7. REFERENCES

- Agarwal, V. and S. Mahadevan, 2014, "Concrete Structural Health Monitoring in Nuclear Power Plants," *Office of Nuclear Energy Sensors and Instrumentation Newsletter*, September 2014.
- Bruck, P., T. Esselman, and M. Fallin, 2012, "Digital Image Correlation for Nuclear," *Nuclear Engineering International*, April 23, 2012.
- Castanedo, F., 2013, "A review of data fusion techniques," *The Scientific World Journal*.
- Hall, D. L. and J. Llinas, 1997, "An introduction to multisensor data fusion," *Proceedings of the IEEE* 85(1): 6–23.
- Christensen, J. A., 1990, "NPAR Approach to Controlling Aging in Nuclear Power Plants," *Proceedings of the 17th Water Reactor Safety Information Meeting*, Washington, D.C., NUREG/CP-0105, Volume 3: 509–529.
- Dean, J. and S. Ghemawat, 2008, "MapReduce: simplified data processing on large clusters," *Communications of the ACM* 51(1): 107–113.
- Farage, M. C. R., J. L. D. Alves, and E. M. R. Fairbairn, 2004, "Macroscopic model of concrete subjected to alkali–aggregate reaction," *Cement and Concrete Research* 34(3): 495–505.
- Gros, X. E., J. Bousigue, and K. Takahashi, 1999, "NDT data fusion at pixel level," *Ndt & E International* 32(5): 283–292.
- Kim, S., D. E. Adams, H. Sohn, G. Rodriguez-Rivera, N. Myrent, R. Bond, J. Vitek, S. Carr, A. Grama, and J. J. Meyer, 2014, "Crack detection technique for operating wind turbine blades using Vibro-Acoustic Modulation," *Structural Health Monitoring* 13(6): 660–670.
- Kobayashi, K. and N. Banthia, 2011, "Corrosion detection in reinforced concrete using induction heating and infrared thermography," *Journal of Civil Structural Health Monitoring* 1(2): 25–35.

- Kokar, M. and K. Kim, 1993, "Review of multisensor data fusion architectures and techniques," in *Intelligent Control*, Proceedings of the 1993 IEEE International Symposium on: 261–266.
- Larive, C., 1997, "Apports combinés de l'expérimentation et de la modélisation à la compréhension de l'alcali-réaction et de ses effets mécaniques," Doctoral dissertation, Ecole nationale des ponts et chaussées.
- Lesnicki, K. J., J.-Y. Kim, K. E. Kurtis, and L. J. Jacobs, 2014, "Characterization of ASR Damage in Concrete using Nonlinear Impact Resonance Acoustic Spectroscopy Technique," *NDT&E International* 44(8): 721–727.
- Liu, Q. C. and H. P. B. Wang, 2001, "A case study on multisensor data fusion for imbalance diagnosis of rotating machinery," *AI EDAM* 15(03): 203–210.
- Lu, Y. and J. E. Michaels, 2009, "Feature extraction and sensor fusion for ultrasonic structural health monitoring under changing environmental conditions," *Sensors Journal, IEEE* 9(11): 1462–1471.
- Mahadevan, S., V. Agarwal, K. Neal, D. Kosson, and D. Adams, 2014, *Interim Report on Concrete Degradation Mechanisms and Online Monitoring Techniques*, INL/EXT-14-33134, Idaho National Laboratory, September 2014.
- Naus, D., 2007, "Activities in Support of Continuing the Service of Nuclear Power Plant Safety-Related Concrete Structures," in *Infrastructure Systems for Nuclear Energy*, T. T. C. Hsu, C.-L. Wu, and J.-L. Li (eds), Chichester, United Kingdom: John Wiley & Sons, Ltd.
- Neiswanger, W., C. Wang, and E. Xing, 2013, "Asymptotically exact, embarrassingly parallel MCMC," arXiv preprint arXiv:1311.4780.
- Quadri, S. A. and O. Sidek, 2014, "Development of heterogeneous multisensor data fusion system to improve evaluation of concrete structures," *International Journal of Image and Data Fusion* 5(2): 97–108.
- Renshaw, J., N. Muthu, and M. Guimaraes, 2014, "Thermographic Inspection of Concrete, Tanks, and Containment Liners," *EPRI Conference*, Charlotte, North Carolina, May 8, 2014.
- Saouma, V. and L. Perotti, 2006, "Constitutive model for alkali-aggregate reactions," *ACI Materials Journal* 103(3): 194.
- Ulm, F. J., O. Coussy, L. Kefei, and C. Larive, 2000, "Thermo-chemo-mechanics of ASR expansion in concrete structures," *Journal of Engineering Mechanics* 126(3): 233–242.